energies

MDPI

*Article*

# Increasing the Metal-Hydride Power Density Using Phase-Change Materials, Advanced Thermal Supports, and Expanded Graphite Nano-Particles

**Marco Maggini [1], Andrea Luigi Facci [1,*], Giacomo Falcucci [2] and Stefano Ubertini [1]**

[1] Department of Economics, Engineering, Society and Business Organization, University of Tuscia, 01100 Viterbo, Italy; marco.maggini@unitus.it (M.M.); stefano.ubertini@unitus.it (S.U.)
[2] Department of Enterprise Engineering Mario Lucertini, University of Rome Tor Vergata, Via del Politecnico 1, 00133 Rome, Italy; giacomo.falcucci@uniroma2.it
* Correspondence: andrea.facci@unitus.it

**Abstract**

The large-scale integration of renewable energy systems requires hydrogen storage technologies that can decouple energy production from energy utilization and allow for seasonal storage. Metal hydrides can offer higher volumetric energy density and operational safety than compressed $H_2$ but are limited by heat-transfer constraints that slow hydrogen absorption and desorption. This work investigates the performance of metal hydride–phase-change material hydrogen storage systems through advanced numerical modeling. Five reactor geometries are evaluated to quantify how longitudinal fins, transversal fins, helical fin structures, and graphite-enhanced composites influence heat removal, charge/discharge rates, and overall power density. Results show that longitudinal and transversal fins accelerate hydrogen absorption and desorption, reducing cycle times by up to 80.6%. The optimized finned helix configuration achieves the highest performance, with a power density of 2.55 kW/kg and charge/discharge powers of 6.75 kW and 13.25 kW, respectively. Expanded graphite further enhances kinetics in low-Biot-number designs, reducing cycle times by more than 30%. These findings provide design guidelines to maximize performance and efficiency of solid-state hydrogen storage for medium- and high-power applications.

**Keywords:** hydrogen technologies; energy systems; hydrogen storage; phase-change material; metal hydrides



Academic Editor: George Avgouropoulos

Received: 7 November 2025
Revised: 19 December 2025
Accepted: 23 December 2025
Published: 29 December 2025



## 1. Introduction

The shift from fossil fuels to Renewable Energy Sources (RES) is essential to meet the ambitious climate energy goals established by the European Commission Energy Roadmap 2050 [1] and the 17 Sustainable Development Goals of the United Nations [2]. Decarbonizing the energy sector poses many technical challenges, in particular for hard-to-abate sectors. In this context, hydrogen has an excellent potential [3,4]. At the same time, hydrogen is a good energy storage medium, since it can provide seasonal storage of large amounts of energy with low losses [5,6], whereas even high-efficiency electrochemical batteries suffer from considerable self-discharge [7]. Hydrogen can be either stored by compression, liquefaction, or ab/adsorption into suitable materials (e.g., Metal Hydrides (MHs)) [8,9].

Among the solid-state storage options, MHs allow safe handling, due to low operating pressures and temperatures, as well as high volumetric densities [9–12]. However, MHs competitiveness with state-of-the-art technologies (namely pressurized hydrogen) is strongly affected by the efficiency of its Heat Management System (HMS). In fact, the absorption of hydrogen into the MH (hydrogenation) and subsequent desorption (dehydrogenation) are exothermic/endothermic reactions, respectively [9]. The reaction rate (and, thus, the charge and discharge time) is strongly dependent on the capacity to remove the absorption heat and provide the desorption heat [13]. Therefore, many Thermal Augmentation Systems (TASs) have been designed and developed (e.g., addition of internal/external fins, modification of the thermal properties of the material by adding high-conductivity powders and/or metal foams, internal and external heat exchangers, and heat pipes). An alternative option is to couple the MH with a phase-change material (PCM) to form an MH–PCM system. The PCM acts as a thermal energy reservoir and as a passive HMS [14,15] that stores absorption heat during the hydrogenation phase and releases the desorption heat during the discharge phase. Although less effective than most heat exchanger-based HMSs, an MH–PCM controls the MH temperature without requiring an external supply of energy (e.g., pumps) [16,17]. This allows the round-trip efficiency of the system not to be reduced.

The PCM must be selected according to the parameters of the chemical reaction. In particular, the melting temperature must be within the equilibrium temperature range of the reaction, while a higher melting enthalpy guarantees better performance in a reduced volume and mass [18,19]. Several researchers have already dived into the experimental and numerical investigation of MH–PCM systems, with the aim of reducing the cycle time and increasing the round-trip efficiency. Table 1 summarizes their contribution.

**Table 1.** Selected literature review of the MH hydrogen storage system with active or passive HMS.

| Author | Metal Hydride | Heat Management System | Geometry | Major Themes |
|---|---|---|---|---|
| Bouzgarrou et al. (2021) [20] | $Mg_2Ni$ | PCM + heat pipes | bare cylinder + U-type tubes | improving performance through increasing heat exchange |
| Mellouli et al. (2024) [21] | $Mg_2Fe$ + $LaNi_5$ | PCM | immersed bare cylinder | pairing two MHs increase the efficiency of a TES unit |
| Dong et al. (2024) [22] | $LaNi_5$ | PCM | bare cylinder with honeycomb fins and sandwich design | optimization of the honeycomb fins inside the MH–PCM to improve kinetics |
| Larpruendrudee et al. (2024) [23] | $Mg_2Ni$ | PCM + heat exchanger | bare cylinder with internal spiral heat exchanger tubes; PCM is used as (i) jacket, (ii) pool bed, (iii) or capsule | increasing heat exchange between MH and PCM by combining active and passive heat management systems |
| Shrivastav et al. (2024) [24] | $MgH_2$ | PCM + fins | bare cylinders + transversal fins | increasing MH kinetics and balancing the system weight |
| Nyamsi et al. (2024) [25] | $AB_2$-type (Ti/Zr-based) | PCM | bare cylinders + fins/immersed design | integration of MH–PCM with Fuel Cell vehicles |
| Bao et al. (2015) [26] | $MgH_2$ | heat exchangers/heat exchangers + fins + graphite | bare/finned cylinder | increasing MH kinetics by improving heat removal rate |
| Maggini et al. (2024) [27] | $LaNi_5$ | PCM | bare cylinder | non-dimensionalization of the hydrogenation process |
| Present work | Hydralloy C5 | PCM/PCM + fins + graphite | bare, finned, and helix-shaped MH tube | improving MH and PCM heat exchange with passive systems |

Bouzgarrou et al. [20] conducted a numerical study on a metal-hydride reactor integrated with phase-change materials and heat pipes to improve hydrogen storage and

thermal management. They investigate the effects of thermal conductivities, melting temperature, convective heat-transfer coefficient, and the number of heat pipes on the hydrogen absorption efficiency. They show that enhancing PCM thermal conductivity, optimizing melting temperature, and increasing the number of heat pipes improve performance. Mellouli et al. [21] investigated a novel thermochemical-latent energy storage system using paired metal hydrides ($Mg_2Fe$ and $LaNi_5$) and phase-change material. A mathematical model assesses factors like the efficiency of heat supply, initial temperatures, and the heat-transfer coefficient. The study demonstrates that the pairing achieves a specific energy storage capacity of 2 MJ/kg of $Mg_2Fe$ and an efficiency of 87.1%, highlighting the high potential of this hydride combination for effective energy storage systems. Dong et al. [22] investigated the performance of a novel MH–PCM reactor with honeycomb fins. The results show that, while the cycle time is reduced in the finned configuration, the energy storage density is reduced. Finally, they present a sandwich MH–PCM reactor, whose cycle time is 84% lower than the design with PCM on the external side of the honeycomb. Larpruenrudee et al. [23] investigated the performance of a metal-hydride storage system using phase-change materials and innovative heat exchanger designs. The study introduces semi-cylindrical coil heat exchangers, with and without central return tubes, and examines their efficiency in hydrogen absorption and desorption processes. Different PCM configurations, such as jackets, pool beds, and capsules, are analyzed for their impact on heat transfer and storage performance. The work demonstrates that combining central return with PCM capsules improves the system thermal performance, reducing absorption and desorption cycle times significantly, thus demonstrating the importance of both active (heat exchangers) and passive (PCM) thermal management strategies for optimizing hydrogen storage systems. Shrivastav et al. [24] explored the design and optimization of a metal-hydride reactor, using $MgH_2$ as the metal hydride and $NaNO_3$ as the phase-change material. The study incorporates copper fins for enhanced heat transfer. Key findings highlight that the integration of fins significantly accelerates hydrogen absorption, with reactors utilizing 10 and 30 fins reducing absorption time by 86.5% and 97.3%, respectively, compared to reactors without fins. The research also introduces a novel performance evaluation criterion, defined as hydrogen absorption relative to system weight. The criterion helps determine the optimal number of fins or other design parameters that maximize the reaction rate without disproportionately increasing the weight. Nyamsi et al. [25] examined the integration of MH–PCM systems in medium-to-high power fuel cell vehicles. The study uses numerical simulations to analyze hydrogen flow dynamics, focusing on factors like PCM properties, operating conditions, and periodic operation modes. Results show that these systems can sustain hydrogen flow rates for fuel cells under varying power demands, demonstrating their adaptability and efficiency for real-world applications. For instance, a 10 kW FC can be fed for 41 min with a $H_2$ utilization factor of 38%. Also, adding 20% of expanded graphite in the MH increases the utilization factor to 47.2%. Bao [26] investigated the performance of metal-hydride reactors in high-temperature thermochemical heat storage. It evaluates five reactor designs, incorporating measures like metal fins and expanded graphite to improve thermal conductivity and reaction rates. The enhanced designs (fins and graphite) reduced absorption time by up to 50% compared to basic configurations, with a more uniform temperature distribution. The best-performing reactor achieved a power density of 23.6 W/kg. The author concludes that compacted hydride-graphite powder is a cost-effective solution for improving reactor performance, while expensive metal fins can be omitted. Maggini et al. [27] explored the design and optimization of hydrogen storage systems that combine metal hydrides with phase-change materials using a generalized non-dimensional mathematical model. The work seeks to enhance the efficiency of hydrogen energy storage. It finds that the length-to-diameter ratio can increase the power

output by a factor of 10 and that the thermal conductivity of both MH and PCM is also critical. The present work leverages the findings of this previous analysis by considering more complex geometries and modifications of the optimized solution, thereby proposed, which is here considered to be the baseline scenario. In particular, we dissect the effects of adding Expanded Natural Graphite (ENG) on the system performance.

This work focuses on quantifying the performance gains achievable through design variations. Using numerical simulations, we evaluate how geometrical features (fins, helical configurations) and material enhancements (PCM buffering, graphite additives) affect hydrogen absorption and desorption rates, cycle duration, and specific power. The aim is to establish performance-oriented design guidelines for MH–PCM storage systems suitable for demanding applications such as fuel cell vehicles and renewable energy integration [28]. To this end, the study evaluates the primary factors that limit the hydrogen–metal-hydride reaction, with particular emphasis on the heat-transfer processes that govern absorption and desorption rates. The results identify the thermal and geometric constraints that define the practical performance limits of each configuration.

The paper is organized as follows: in Section 2 we describe the methodology, including the heat-transfer model, the domain discretization, and the governing equations. Results are presented in Section 3 and discussed and compared to relevant literature in Section 4. Finally, Section 5 draws the conclusions.

## 2. Methodology

### *2.1. Problem Statement*

In this paper, we investigate the absorption and desorption characteristics of an MH–PCM hydrogen storage system via numerical simulations. We select the alloy Hydralloy $C_5$ ($Ti_{0.95}Zr_{0.05}Mn_{1.46}V_{0.45}Fe_{0.09}$), with a porosity $\xi_m = 0.5$ as supplied by GfE Alloys (AMG Titanium) [29]. Five geometrical configurations are analyzed (see Figure 1), with the same hydride volume and, therefore, the same $H_2$ storage capacity. Case A is a bare cylindrical configuration where the MH (radius $b_1$) is surrounded by an external jacket of PCM (radius $b_2$). A central porous artery (radius $b_a$) distributes the hydrogen gas inside the MH. Such a design is based upon previous research of the authors (cfr. [27]), where they find a recommended configuration to store 1 kWh of energy. Case B and Case C retain the baseline geometry of Case A, with the addition of longitudinal fins in Case B and transversal fins in Case C. Case D is also based upon previous research (cfr. [30]), where a helix-shaped MH tube is found to significantly reduce the cycle time of the reactor. Finally, Case E expands such geometry by adding transversal fins to the external surface of the helix. Table 2 includes the geometric parameters of all the five configurations. The present study also investigates the effect of introducing expanded graphite in the MH and in the PCM as a thermal conductivity enhancer.

We assume ideal thermal insulation of the external wall of the canister (see [31,32], for instance). The central artery (radius $b_a$) is unnecessary for configurations D and E due to the smaller tube diameter. In fact, the diffusion of $H_2$ is hindered only when the gas diffusion distance is too big, according to Equation (1) introduced in [33]:

$$N = \frac{k_e \cdot M_{H_2} \cdot L_{gas}^2 \cdot \mu_{H_2}}{\frac{\partial P_{eq}}{\partial T} \cdot \Delta H \cdot \rho_{H_2} \cdot K \cdot L_{heat}^2}, \quad (1)$$

where $L_{gas}$ and $L_{heat}$ are the gas and heat diffusion distances, respectively. $K$, $\mu$, and $M$ are the MH permeability, hydrogen viscosity, and molecular weight.

Whenever $N \ll 1$, hydrogen can diffuse easily inside the MH porous powder. In our case, $N$ is much smaller than unity for all the designs.

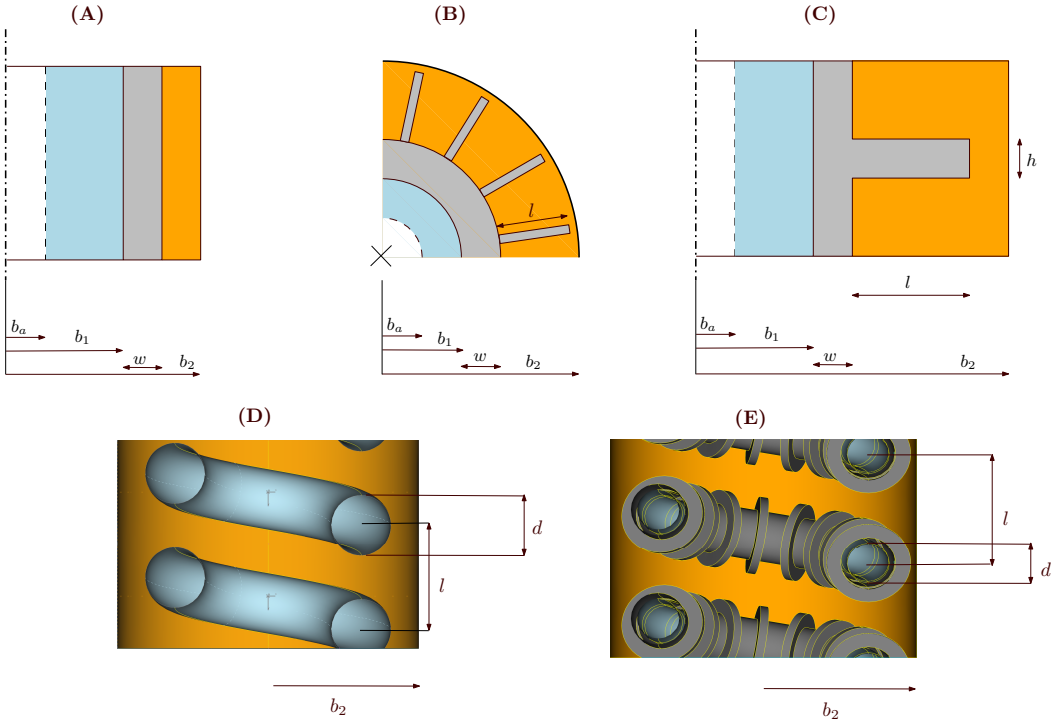


**Figure 1.** Schematics of cases (**A**) (base cylinder), (**B**) (longitudinal finned cylinder), (**C**) (transversal finned cylinder), (**D**) (base helix), and (**E**) (transversal finned helix).

**Table 2.** Geometric parameters of the five configurations. $V$ = volume; $\mathcal{S}$ = heat exchange surface area; $m$ = mass. See Figure 1 for geometrical parameters.

| | Case | | | | | Unit |
|---|---|---|---|---|---|---|
| | **A** Bare Cylinder | **B** Longitudinal Fins | **C** Transversal Fins | **D** Helix | **E** Finned Helix | |
| $d = 2b_1$ | 25.4 | 25.4 | 25.4 | 16 | 10 | mm |
| $\mathcal{L}$ | 1200 | 1200 | 1200 | 532 | 1372 | mm |
| $b_2$ | 35.7 | 36.7 | 39.7 | 52.5 | 16.75 | mm |
| $b_a$ | 5 | 5 | 5 | - | - | mm |
| $V_{MH}$ | 602.1 | 602.1 | 602.1 | 601.8 | 607.2 | $cm^3$ |
| $V_{PCM}$ | 3875 | 3783 | 2800 | 4030 | 4230 | $cm^3$ |
| $\mathcal{S}$ | 0.118 | 0.787 | 0.928 | 0.152 | 0.637 | $m^2$ |
| $m_{H_2}$ | 34.9 | 34.9 | 34.9 | 34.9 | 35.2 | g |
| $w$ | 3 | 3 | 3 | - | 3 | mm |
| $h$ | - | 2 | 2 | - | 2 | mm |
| $l$ | - | 24 | 20 | 28 | 28 | mm |

The hydrogen inlet (absorption) pressure $p^a$ is set to 40 bar in all tests, while the outlet (desorption) pressure $p^d$ is set to 1 bar.

The MH is inserted in an aluminum vessel of thickness $w = 3$ mm, surrounded by an external jacket of paraffin wax as PCM, whose fusion temperature range is equal to 302 K (solid) and 304 K (liquid). Such a temperature range is within the absorption and desorption lower/upper temperature limits of the reaction.

### *2.2. Mathematical Modeling*

The following hypotheses are considered in the simulations:

- ideal gas law is applied for hydrogen, i.e., $p_{H_2} = \frac{m_{H_2} RT}{V}$ (see for instance [33]);
- the MH porosity is homogeneous (see for instance [34]);
- the thermophysical properties of the MH and the PCM are constant with temperature [35];

- local thermal equilibrium is applied inside the MH, i.e., $T_{MH} = T_{H_2}$ at any instant and in any point of the domain (see [36]).

Notably, the momentum conservation equations can be neglected, allowing for a much faster simulation without losing accuracy [33]. In fact, if the pressure gradient within the MH domain is negligible (see Section 2.1), the diffusion of the hydrogen gas is virtually instantaneous.

#### 2.2.1. MH Modeling

We model the systems described in Section 2 through the energy conservation equation. In particular, in the MH domain, the equation reads [37]:

$$(\rho c_p)_e \frac{\partial T}{\partial t} = k_e \nabla^2 T + \dot{q}, \tag{2}$$

where $k_e$ is the effective thermal conductivity of the MH, $(\rho c_p)_e$ is the effective heat capacity of the MH, and $\dot{q}$ is the volumetric reaction heat source inside the MH [W/m$^3$]. The absence of the convective term in the energy conservation equation is justified by the small value of $N$, as discussed above. This assumption was already debated in the literature and confirmed in [36]. In turn, $k_e$ and $(\rho c_p)_e$ are evaluated as follows:

$$k_e = \xi_m k_{H_2} + (1 - \xi_m) k_m, \tag{3a}$$

$$(\rho c_p)_e = \xi_m \rho_{H_2} c_{pH_2} + (1 - \xi_m) \rho_m c_{pm}. \tag{3b}$$

The Hydralloy thermal conductivity, density, and specific heat are $k_m$ = 1.6 W/mK, $\rho_m$ = 6400 kg/m$^3$, $c_{pm}$ = 434 J/kgK [38]. $f_{H_2}$ is the hydrogen mass flow rate, which is positive during absorption (charge), and negative during desorption (discharge).

During absorption, the reaction rate $r$ [s$^{-1}$] is [37]:

$$r = C_a e^{-\frac{E_a}{RT}} \ln \frac{p}{p_{eq}} \left(1 - \frac{m_{MH}}{m_t}\right), \tag{4}$$

while in desorption:

$$r = C_d e^{-\frac{E_d}{RT}} \frac{p - p_{eq}}{p_{eq}} \left(\frac{m_{MH}}{m_t}\right). \tag{5}$$

The equilibrium pressure $p_{eq}$ reads:

$$p_{eq} = p_0 \, e^{\left[\frac{\Delta H}{RT} - \frac{\Delta S}{R} + \beta\left(\frac{m_{MH}}{m_t} - \frac{1}{2}\right)\right]}, \tag{6}$$

where $p_0$ = 1 bar is the reference pressure, $\Delta H$ and $\Delta S$ are the enthalpy, entropy variations, respectively.

The volumetric heat source term, to be used in Equation (2), is:

$$\dot{q} = -\Delta H \cdot r \cdot (\xi \cdot \rho_{MH}) \cdot \frac{S_c}{M_{MH}}, \tag{7}$$

where $S_c$ is the stoichiometric ratio of the metal hydride (equal to 0.48).

When graphite is inserted in the MH to increase $k_e$, the following formulation is used [39]:

$$k_e = \left( k_{ENG} \frac{\frac{m_{ENG}}{\rho_{ENG}}}{\frac{m_{ENG}}{\rho_{ENG}} + \frac{m_{MH}}{\rho_{MH}}} + k_m \frac{\frac{m_{MH}}{\rho_{MH}}}{\frac{m_{ENG}}{\rho_{ENG}} + \frac{m_{MH}}{\rho_{MH}}} \right) \cdot (\xi_m + \xi_{ENG}). \tag{8}$$

2.2.2. PCM Modeling

Conduction inside the PCM is modeled through the enthalpy method, according to [40]:

$$\rho_{\mathrm{PCM}} \frac{\partial H}{\partial t} = k_{\mathrm{PCM}} \nabla^2 T \tag{9}$$

where $H = c_p T$ is the enthalpy and the relationship between $H$ and the temperature inside the PCM is:

$$T = \begin{cases} H/c_{p,\mathrm{PCM}}, & H \leq c_p T_{\mathrm{m}} \\ T_{\mathrm{m}}, & c_p T_{\mathrm{m}} < H \leq c_p T_{\mathrm{m}} + \lambda \\ (H-\lambda)/c_p, & H > c_p T_{\mathrm{m}} + \lambda \end{cases} \tag{10}$$

Convection inside the PCM is disregarded, since conduction dominates heat transfer (see [30,41]). In fact, convection can moderately affect the temperature, while not impacting the power exchanged between the MH and the PCM [30,41]. Furthermore, this is a conservative assumption since considering the convection will increase the heat-transfer rate and, thus, the PCM effectiveness. We note that the geometries and operating conditions herein considered are based on the results of [30]. Therefore, further analysis of the natural convection effects is unnecessary.

This work considers the mixing of expanded graphite with the PCM powder to increase the heat-transfer rate [42] and, thus, the kinetics of the reaction. We use Maxwell's formulation [43] to derive the effective thermal conductivity of a PCM matrix embedded with ENG inclusions:

$$k^e_{\mathrm{PCM}} = k_{\mathrm{PCM}} \left[ 1 + \frac{3\phi}{\left( \frac{k_{\mathrm{ENG}} + 2k_{\mathrm{PCM}}}{k_{\mathrm{ENG}} - k_{\mathrm{PCM}}} \right) - \phi} \right], \tag{11}$$

where $\phi$ is the volume fraction of the inclusions and $k_{\mathrm{ENG}}$ is the graphite conductivity. This formula is only valid and stable for $\phi < 0.25$ [43].

*2.3. Numerical Solution and Boundary Conditions*

The numerical solution of Equations (2), (4), (5) and (10) is obtained through AnSys Fluent 2022 R2 [44]. The specific chemical model is implemented through custom UDFs. We use a finite-volume method, with the least square-based approach to approximate the gradients and the first-order Euler implicit scheme for the temporal integration. The MH–PCM interface is modeled through a coupled wall thermal boundary condition. Mesh size and timestep are discussed in Section 2.5. For the simulations, the parameters shown in Table 3 were used. The total simulation time is set to 1 h for both absorption and desorption processes.

Cases A, B, and C present axial symmetry, with Cases B and C also presenting circular and translational periodicity, respectively. Furthermore, ideal insulation was considered for the external wall. Therefore:

$$\left. \frac{\partial T}{\partial b} \right|_{b=0} = \left. \frac{\partial T}{\partial b} \right|_{b=2} = 0 \tag{12}$$

and only the periodic portion of the global domain is modeled in Cases B, C, D, and E. Specifically, Cases A, B, and C are modeled in two dimensions, whereas Cases D and E

need 3D modeling, since they do not benefit from axial symmetry. The assumption of ideal insulation is also applied in the longitudinal direction. Therefore:

$$\left.\frac{\partial T}{\partial z}\right|_{z=0} = \left.\frac{\partial T}{\partial z}\right|_{z=\mathcal{L}} = 0. \tag{13}$$

For Cases B and C, we use a two-side coupled wall boundary condition to model the heat transfer at the MH-Fin and the Fin-PCM interfaces. Such boundary conditions proxy the heat transfer through finned surfaces by switching the thermal conductivity value.

**Table 3.** Coefficients and properties of the alloy Hydralloy $C_5$, used in the calculations. $S_c$ is derived by the authors.

| Parameter | Value | Unit | Reference |
|---|---|---|---|
| $C_a$ | $4 \times 10^6$ | $s^{-1}$ | [45] |
| $C_d$ | $4 \times 10^6$ | $s^{-1}$ | [45] |
| $\Delta H_a$ | $-23{,}500$ | $J{\cdot}mol^{-1}$ | [45,46] |
| $\Delta H_d$ | 28,000 | $J{\cdot}mol^{-1}$ | [45,46] |
| $\Delta S_a$ | $-103$ | $J{\cdot}mol^{-1}\ K^{-1}$ | [45,46] |
| $\Delta S_d$ | 103 | $J{\cdot}mol^{-1}\ K^{-1}$ | [45,46] |
| $E_a$ | 40,000 | $J{\cdot}mol^{-1}$ | [45] |
| $E_d$ | 40,000 | $J{\cdot}mol^{-1}$ | [45] |
| $p_0$ | 1 | bar | |
| $\beta$ (abs/des) | 0.72/0.53 | - | [46] |
| $S_c$ | 0.48 | - | |

We consider the initial conditions reported in Table 4.

**Table 4.** Initial conditions utilized in numerical simulations.

| Absorption Phase | Desorption Phase |
|---|---|
| $T_{MH} = T_{PCM} = 298\,K$ | $T_{MH} = T_{PCM} = T_m$ |
| $p = p_{eq,298\,K} = 12.7\,bar$ | $p = p_{eq,T_m} = 15.3\,bar$ |
| $\frac{m_{MH}}{m_t} = 0$ | $\frac{m_{MH}}{m_t} = 1$ |

### *2.4. Model Validation*

We compare the results of our model in absorption and desorption with data from Laurencelle et al. [47]. Two experiments are taken as reference, named "small reactor" and "large reactor", respectively. The first comprises 1 g of $LaNi_5$ and is charged/discharged at 6/0.068 bar, while the second contains 25 g of $LaNi_5$ and is charged/discharged at 12.7/0.086 bar. The small reactor is kept at constant temperature in an oven, while the large reactor comprises convective cooling of the external walls with water. The validation results are shown in the previous work of the authors [30], of which this paper is a natural continuation, and are not here repeated.

Table 5 reports the parameters used for validation [37].

**Table 5.** Parameters used for the model validation, where $LaNi_5H_6$ is selected as MH [47].

| Parameter | Value | Unit |
|---|---|---|
| $C_a$ | 59.2 | $s^{-1}$ |
| $C_d$ | 9.6 | $s^{-1}$ |
| $\Delta H_a$ | −30,478 | $J \cdot mol^{-1}$ |
| $\Delta H_d$ | 30,800 | $J \cdot mol^{-1}$ |
| $\Delta S_a$ | −108 | $J \cdot mol^{-1}\ K^{-1}$ |
| $\Delta S_d$ | 108 | $J \cdot mol^{-1}\ K^{-1}$ |
| $E_a$ | 21,170 | $J \cdot mol^{-1}$ |
| $E_d$ | 16,420 | $J \cdot mol^{-1}$ |
| $p_0$ | 1 | bar |
| $\beta$ | 0.13 | - |
| $S_c$ | 3 | - |

### *2.5. Mesh Sensitivity*

Table 6 reports the results of the mesh and timestep sensitivity analyses conducted for Case C (transversal finned canister). As a result, a mesh of 1060 and a constant timestep of 10 ms are chosen for all the simulation tests. Notably, an adaptive timestep could not be implemented since the Courant number is meaningless when the flow equations are not considered.

**Table 6.** Mesh and timestep sensitivity analysis, performed on Case C (transversal finned canister).

| Mesh | $H_2$ Capacity (t = 1 h) | Liquid Fraction (t = 1 h) |
|---|---|---|
| 254 | 88.06% | 9.9% |
| 640 | 88.13% | 9.9% |
| 1060 | 88.15% | 9.9% |
| 1568 | 88.16% | 9.9% |
| t-step | | |
| 5 ms | 88.15% | - |
| 10 ms | 88.15% | - |
| 20 ms | floating point exception | |
| 100 ms | floating point exception | |

## 3. Results

Figure 2 shows the $H_2$ storage level, PCM liquid fraction, MH–PCM heat-transfer rate, and MH average temperature for the five cases analyzed during the absorption phase. Case A is the slowest configuration and does not achieve complete hydrogenation in 1 h (it reaches 99.5% in 6517 s). Finned configurations (Cases B and C) have almost identical performances, with complete hydrogenation (set to 99.5%) in 1220 and 1271 s, respectively. This is explainable by considering that $\mathcal{S}$ (heat exchange surface area between MH and PCM) is much larger in the finned cases than in Case A (see Table 2), thus fostering faster energy transfer from the MH to PCM. Case D (non-finned helix) exhibits a faster hydrogenation than the base cylinder, but a slower one compared to the finned cylinders (Cases B and C). In fact, $\mathcal{S}$ is only marginally higher for Case D than for Case A, while it is much higher for Cases B and C. This leads to a slower heat-transfer rate compared to the finned cylinders. It reaches complete absorption in 5173 s. Finally, the finned helix design (Case E) shows the fastest hydrogenation, achieved in only 625 s.

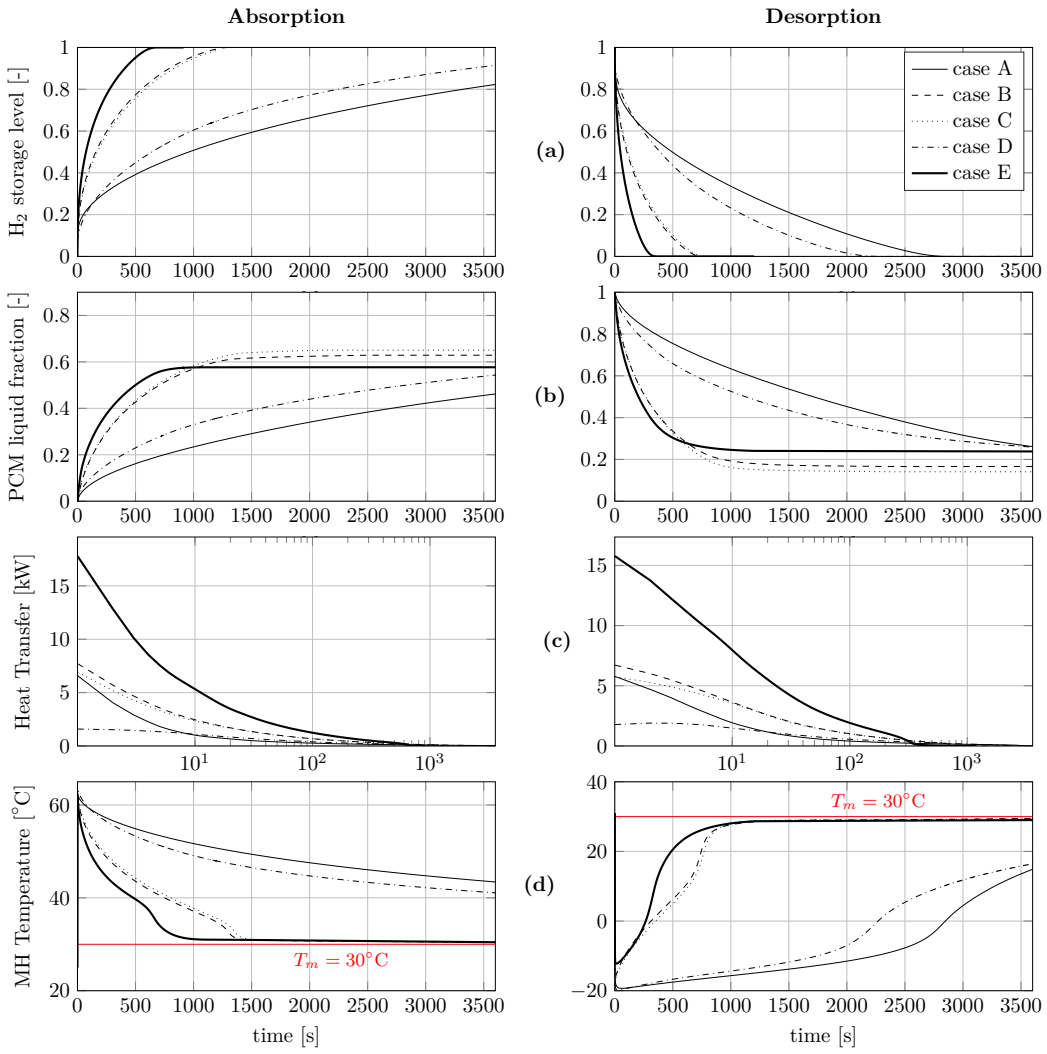


**Figure 2.** Hydrogen storage capacity (**a**), PCM liquid fraction (**b**), heat-transfer rate between MH and PCM (**c**), and MH average temperature (**d**) in Absorption and Desorption.

The PCM does not reach complete liquefaction in any of the configurations, since the hydrogenation enthalpy is lower than the de-hydrogenation one. Thus, the PCM amount is calibrated on the discharge phase, where more heat must be provided to the MH. Furthermore, a part of the heat developed during the charge is stored in the aluminum walls and fins, and in the PCM in the form of sensible heat, since the initial temperature $T_i = 298\,\mathrm{K} < T_m = 302\,\mathrm{K}$. Therefore, the PCM only receives a fraction of the hydrogenation enthalpy. Cases B and C exhibit almost identical liquefaction front progressions, reaching a value of ≈60% when complete hydrogenation is achieved. However, the liquefaction continues after complete hydrogenation, since the MH average temperature is not yet in equilibrium. Case D has a slower liquefaction front than for Cases B, C, and E, accordingly to the above-mentioned analysis of the hydrogen storage capacity evolution. Case E shows a final PCM liquid fraction slightly below 60% when, consistently, the temperature has reached $T_m$ again.

In terms of heat-transfer rate, Case E exhibits the highest heat-transfer rate, as expected, since it is the fastest design. All the designs present a high initial peak, between 2 and 17.5 kW, and a gradual reduction with time. Cases A and D are the least effective in exchanging heat with the PCM, which explains why they are the slowest configurations.

Case E shows a steep and rapid temperature decrease, consistently with the rapid chemical reaction. Despite the highest temperature reached being essentially the same

in the five cases (i.e., around 62.5 °C), Cases A and D present a very slow and gradual cooling, while Cases B and C are in between. The initial steep increase in temperature is due to a very high reaction rate, thanks to a low initial temperature. The maximum temperature is reached when $p_{eq} = p_{H_2}$, i.e., when the equilibrium pressure caps the hydrogen supply pressure.

During the desorption phase (see Figure 2), the temperature decreases, and heat is transferred from the PCM to the MH. Case A achieves complete discharge (0.5% in $H_2$ content) in 2700 s and it is the slower among the five configurations. Cases B and C achieve similar performance and reach complete discharge in 700 s both. Case D is slower than the finned designs, though faster than the basic cylinder, achieving complete desorption in 2119 s. Case E, finally, is the faster, reaching 0.5% in energy content in only 320 s.

PCM liquid fraction reaches a minimum of ≈18 ÷ 23% for all cases, though for Case A, this is not a stable value, since the MH temperature has not reached the equilibrium at this point (see Figure 2d). For Case E, conversely, it is a stable value, since the MH temperature has almost reached $T_m = 30$ °C again. A minimum temperature of about −20 °C is reached in the very first seconds of reaction for Cases A and D, while Cases B and C reach a minimum temperature of around −16 °C. Case E, finally, reaches a minimum of about −10 °C, thanks to a more efficient heat exchange. The average temperature of Cases B, C, and E rapidly rises again after the minimum is reached, while Cases A and D are much slower, due to a lower conduction rate.

Case E presents the higher heat-transfer rate (Figure 2c), peaking to 16 kW, while Case D presents the lower one, at 2 kW. In all cases, the heat-transfer rate peaks in the initial brief phase and then reduces with time, as the temperature gradient between MH and PCM reduces.

Table 7 summarizes the results in terms of ab-desorption cycle time (99.5% and 0.5% for absorption and desorption, respectively), PCM liquid fraction at the end of the reaction, and maximum-minimum temperature reached during the cycle.

**Table 7.** Results of the ab-desorption cycle for the five configurations proposed, with $T_m = 30$ °C. * at the end of absorption − desorption.

| Case | abs. Time [min] | des. Time [min] | PCM Liquid Fraction [%] * | Max. Temperature [°C] | Min. Temperature [°C] |
|---|---|---|---|---|---|
| A | 108.6 | 45.3 | 62.2 − 26.1 | 62.5 | −19.4 |
| B | 20.3 | 9.5 | 61.2 − 20.3 | 62.5 | −16.0 |
| C | 21.7 | 11.6 | 61.2 − 20.3 | 62.5 | −16.5 |
| D | 82.2 | 35.3 | 63.9 − 25.9 | 62.5 | −20.0 |
| E | 10.4 | 5.3 | 57.0 − 24.0 | 62.0 | −12.3 |

### 3.1. *Effect of the* PCM *Selection*

Figure 3 shows the charge and discharge performance for the five configurations when $T_m = 44$ °C, i.e., when using a different PCM with a higher melting point. A higher $T_m$ increases the equilibrium pressure plateau. In this case, none of the configurations reaches a hydrogen storage capacity of 100% within 1 h. The increase in absorption time is due to the higher equilibrium pressure, which slows down the reaction. In fact, the pressure term in Equation (4) is now lower. Case E also reaches a constant value of ≈81%, without any further significant advancement. Consistently, the PCM liquid fraction also reaches a constant value. These results show that the hydrogen supply pressure must increase beyond 40 bar to allow complete absorption at 44 °C.

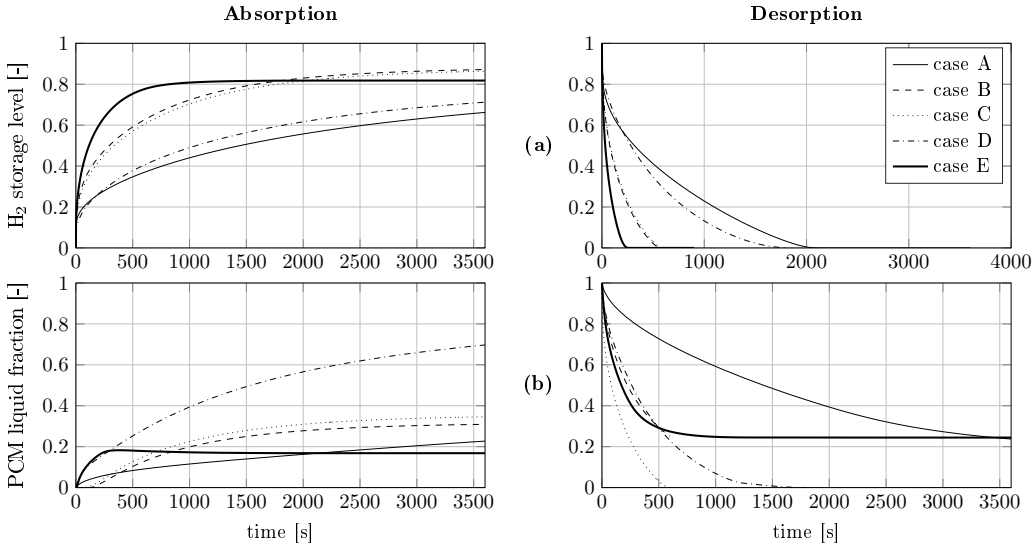


**Figure 3.** Hydrogen storage capacity (**a**) and PCM liquid fraction (**b**) in Absorption and Desorption with $T_m = 44$ °C.

Conversely to absorption, the desorption phase is faster when increasing the PCM melting temperature to $T_m = 44$ °C (see Figure 3). The discharge is accomplished in all cases within 30 min, with Cases B and C reaching 0.5% in hydrogen content in ≈545 s. Case E achieves complete desorption in just 230 s. In fact, conversely to the charge phase, increasing the temperature facilitates the discharge of hydrogen from the MH. This is due to a higher $p_{eq}$ and, according to Equation (5), the reaction rate is higher if $p \ll p_{eq}$. The results show the importance of selecting the proper PCM according to which of the two phases is crucial.

### *3.2. Effect of ENG in the PCM*

The storage performance, in terms of hydrogen flow rate, heat exchange, and temperature management, can be enhanced by improving the thermophysical properties of the MH and the PCM. This can, in turn, be achieved by adding expanded graphite to the PCM. By increasing the volume fraction of ENG inside the PCM ($\phi$) of Case A, the $H_2$ absorption is faster (see Figure 4). In particular, the $H_2$ storage capacity is 5.4% higher at t = 1 h when $\phi = 10\%$ and 10% higher when $\phi = 25\%$. At the same time, the PCM liquid fraction increases by 36.17% and 56.68%, respectively. This is a result of the decrease in the latent heat of fusion in the material, according to the formula:

$$\lambda^* = \lambda \cdot (1 - \phi), \tag{14}$$

where $\lambda^*$ is the new latent heat of fusion of the PCM, after ENG has been added.

Figure 4 shows that the desorption phase is also positively affected by the introduction of ENG in the paraffin, with a reduction of up to −31.22% in desorption time when $\phi = 25\%$. At the same time, the PCM liquid fraction decreases by 29.86% (Equation (14)).

However, the impact of ENG in the PCM varies significantly depending on the geometry of the storage system. Figure 5 shows the absorption and the desorption phase (MH fraction and PCM liquid fraction) in Case C when ENG is inserted in different amounts. Conversely to Case A, Case C is not affected by $\phi$, since there is no appreciable variation in the MH fraction as $\phi$ increases. In fact, even when $\phi = 25\%$, the reaction is only 0.43% faster than the baseline case in absorption and 4.8% faster in desorption. However, the PCM liquid fraction significantly increases in charge and decreases in discharge, as a result of a reduction in $\lambda$.

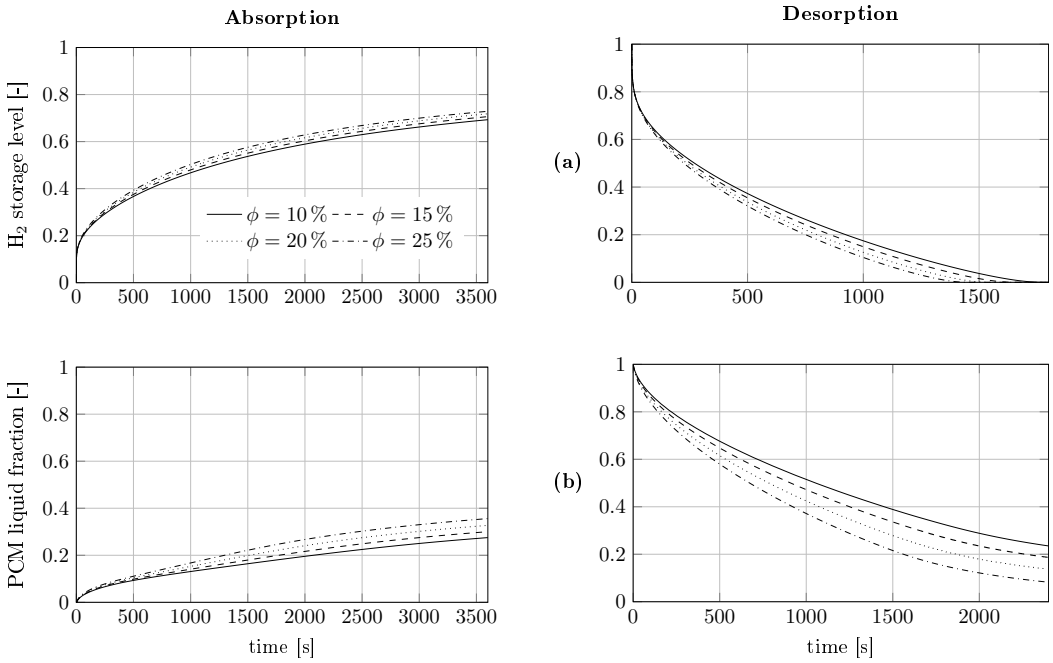


**Figure 4.** Hydrogen storage capacity (**a**) and PCM liquid fraction (**b**) in Absorption and in Desorption for Case A when ENG is inserted in the PCM in different amounts ($\phi$).

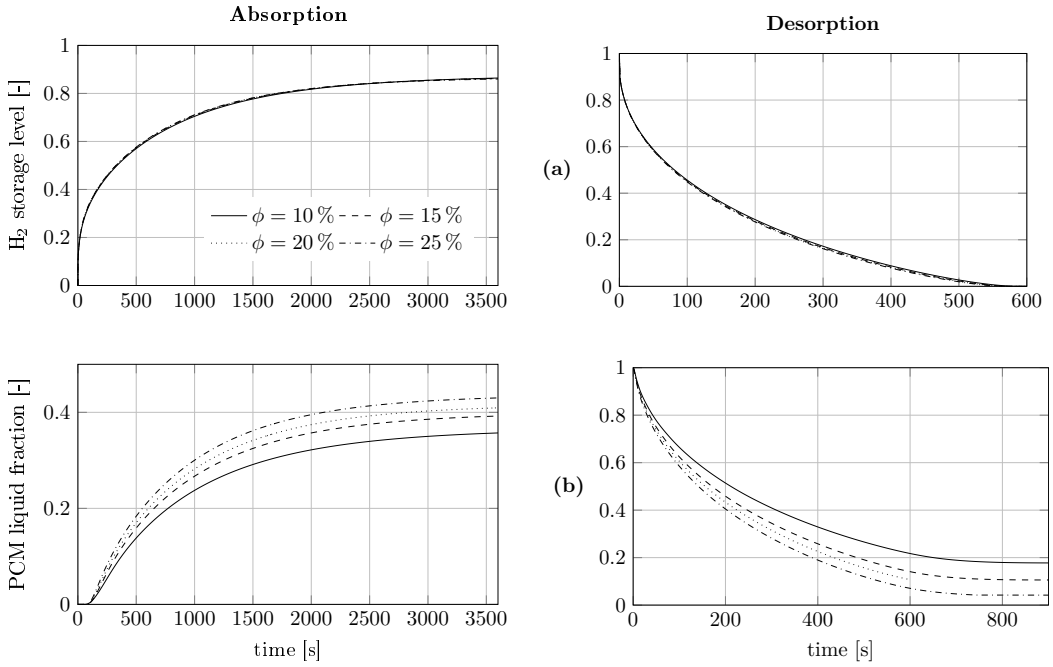


**Figure 5.** Hydrogen storage capacity (**a**) and PCM liquid fraction (**b**) in Absorption and in Desorption for Case C when ENG is inserted in the PCM in different amounts ($\phi$).

### *3.3. Effect of ENG in the MH*

It is possible to increase the MH thermal conductivity by inserting expanded graphite, copper/aluminum oxides, or metal foams. An increase in $k_m$ leads to a decrease in the cycle time of the reaction. For instance, by inserting ENG in the MH, the effective thermal conductivity can reach about 20 W/mK, with values as high as 40 W/mK for the radial conductivity being reported in experimental literature [39]. In fact, by mixing 15% in mass fraction of ENG (i.e., 0.289 kg) with 1.93 kg Hydralloy and using the formulations expressed in [39], we obtain an effective thermal conductivity of 25.91 W/mK inside the MH. Figure 6 shows the absorption phase of Case C when 15% (in mass fraction) of ENG is inserted

in the MH. The absorption time reduces to 308 s (−76.8%) compared to simple Case C. The desorption time is 159 s (−77.1%). Overall, the cycle time is thus reduced by 76.7% in comparison to the Case C without ENG.

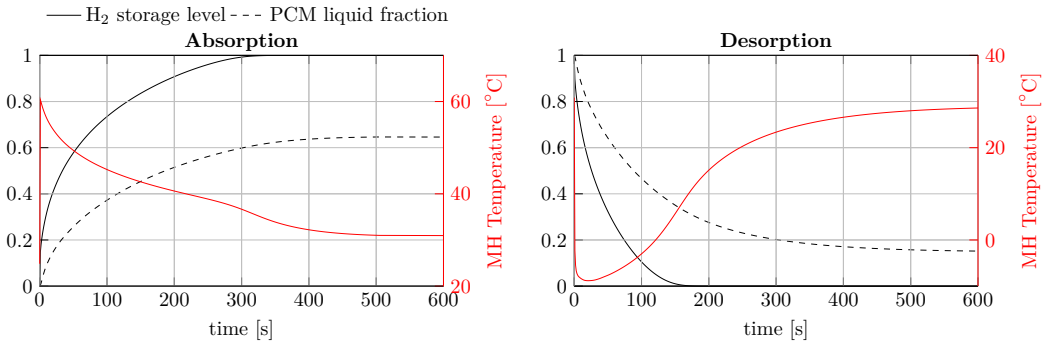


**Figure 6.** Absorption and Desorption of Case C where the MH conductivity $k_m$ is set to 25.91 W/mK, i.e., $\phi = 15\%$ in the MH.

In Case A, the reduction is −12.1% in absorption (95.4 min) and −17.8% in desorption (37.2 min), when $\phi$ is 15% inside the MH. The reduced impact of ENG in Case A compared to Case C is due to the different heat-transfer rates inside the MH and the PCM. In Case C, the fins increase the heat exchange at the surface, whereas the heat flows slowly inside the MH. Thus, increasing the conductivity of the alloy has a significant impact on the total heat-transfer rate. Conversely, in Case A, the conductivity at the MH–PCM surface and inside the MH is not significantly different. This aspect will be further discussed in Section 4.

We comment that, while inserting ENG in the MH also increases the performances, it will lead to a reduction in the hydrogen storage capacity due to a reduced volume fraction of the MH in the canister, which is not the case when improving the properties of the PCM only.

## 4. Discussion

In Case A, the thermal diffusivity of the PCM is a limiting factor of the reaction, since an increase in $\phi$ yields better performances (i.e., a reduced cycle time). In this case, the heat exchange surface between MH and PCM is not enhanced with the installation of external fins. Cases B and C, conversely, significantly increase such surface area. This leads to more effective heat exchange between the MH and the PCM. As a result, the potential benefit of adding ENG to the PCM becomes negligible because the PCM's thermal diffusivity is no longer the limiting factor (see Figure 5). At this stage, storage performance can be improved only by increasing the diffusivity of the MH (see Figure 6). This shows that the convenience of ENG strongly depends on the geometry of the storage system.

We define the equivalent Biot number $\mathrm{Bi}_e$ as:

$$\mathrm{Bi_e} = U_e \cdot d / k_e. \tag{15}$$

Since we simulate a purely conductive heat transfer between the MH and PCM, the equivalent heat-transfer coefficient $U_e$ [W/m$^2$K] can be derived from:

$$\dot{Q} = U_e A (T_s - T_{\mathrm{ref}}), \tag{16}$$

where $\dot{Q}$ is the heat-transfer rate at the MH–PCM surface [W], $T_s$ is the surface temperature of the MH, $T_{\mathrm{ref}}$ is a reference value taken equal to the temperature of the PCM far from the MH–PCM surface, and $A$ is the heat-transfer surface area of the MH domain. We then

evaluate the average heat-transfer coefficient $\overline{U_e}$ and Bi number $\overline{\mathrm{Bi_e}}$ for each configuration to evaluate which cases present a value lower than 0.1 (see Table 8). The lower the Bi number, the lower is the temperature gradient inside the MH, between $b_a$ and $b_1$ (in Cases A, B, and C) or between $b = 0$ and $b_1$ (in Cases D and E) [48,49]. The introduction of ENG in the PCM of Cases A and C leads to an increase in the Bi number, thus to a less homogeneous temperature distribution inside the MH. This is in accordance with Figures 4 and 5, where enhancing the PCM thermal conductivity shows no enhancement in the reaction's kinetics in Case C and a slight improvement in Case A. In fact, Case A with no enhancement has a rather low Bi number, entailing greater possibilities of improvement, while Case C already has a rather high conductive heat transfer at the MH–PCM interface. The helix-shaped designs (Cases D and E) exhibit lower Bi values than Cases B and C, in line with Case A.

For comparison, by introducing 15% of ENG in the PCM in Case E, we observe a 19.0% reduction in absorption time, i.e., to reach 99.5% of $H_2$ storage capacity, while we observe a 13.5% reduction in desorption time. Therefore, a lower Bi number entails a larger enhancement margin by improving the PCM thermal properties, whereas a high Bi number shows a capped limit on the PCM heat-transfer rate (e.g., Case C).

When inserting ENG in the MH in Case C, the average $\mathrm{Bi_e}$ number $\overline{\mathrm{Bi_e}}$ decreases dramatically to 0.45 in absorption (−97.3%), clearly showing the huge effect of the MH conductivity on the heat-transfer rate. Consistently, when we insert ENG in the MH in Case A, the cycle time reduction is less evident (−13.8%), due to an already low starting value of $\overline{\mathrm{Bi}}$, which still reduces to 0.030 in absorption (−96.6%).

**Table 8.** Heat-transfer coefficient and Bi number for each configuration during the absorption phase.

| | $A$ [m$^2$] | $\overline{U_e}$ [$\frac{\mathrm{W}}{\mathrm{mK}}$] | $\overline{\mathrm{Bi_e}}$ |
|---|---|---|---|
| Case A | 0.0958 | 31.2 | 0.897 |
| Case B | 0.0958 | 620.8 | 17.9 |
| Case C | 0.0958 | 570.9 | 16.4 |
| Case D | 0.152 | 22.3 | 0.404 |
| Case E | 0.130 | 103.9 | 1.18 |
| Case A ($\phi = 20\%$ in PCM) | 0.0958 | 49.3 | 1.42 |
| Case C ($\phi = 20\%$ in PCM) | 0.0958 | 761.8 | 21.9 |
| Case A ($\phi = 15\%$ in MH) | 0.0958 | 30.5 | 0.030 |
| Case C ($\phi = 15\%$ in MH) | 0.0958 | 459.6 | 0.451 |

The volumetric density is 7.24 $\mathrm{kg_{H_2}/m^3}$ for Case A, 5.86 $\mathrm{kg_{H_2}/m^3}$ for Case B, 6.85 $\mathrm{kg_{H_2}/m^3}$ for Case C, 7.55 $\mathrm{kg_{H_2}/m^3}$ for Case D, and 6.13 $\mathrm{kg_{H_2}/m^3}$ for Case E. Therefore, the introduction of fins reduces the energy density as expected, since a part of the original volume is now occupied by the aluminum fins. Cases A, B, C, D, and E exhibit an average discharge power of 1.53 kW, 7.33 kW, 6 kW, 1.97 kW, and 13.25 kW, respectively. As for the power densities, they are: 0.31 kW/kg, 1.51 kW/kg, 1.23 kW/kg, 0.39 kW/kg, and 2.55 kW/kg, respectively. In charge, the average powers are: 0.64 kW, 3.43 kW, 3.21 kW, 0.85 kW, and 6.75 kW, respectively. Overall, the discharge power results in 52.74% ± 4.98% lower than the charge power, due to the relatively high $p_{eq}$ at $T_m$.

The authors made similar calculations with $LaNi_5$ as a metal alloy in previous works [30], finding that the charge average power for small-scale storage systems is higher than the average discharge power. In fact, $LaNi_5$ has a lower equilibrium pressure than Hydralloy in the same temperature range, thus facilitating the absorption and hindering the desorption stage. Therefore, tailoring the appropriate material for the hydrogen absorption to the specific application is pivotal. For instance, mobile applications require very high power densities, thus suggesting that Hydralloy would be better than $LaNi_5$ in this context.

Introducing 20% Vol. fraction in the PCM (cost $\approx$ 450 €/kg) reduces the cycle time by 30.8% in Case A, and by 4.72% in Case C. For comparison, adding 16 longitudinal fins ($h = 2$ mm, $l = 24$ mm) adds a negligible cost for the fins manufacturing while reducing the cycle time of Case A by 80.64%. Adding transversal fins with a 12 mm step reduces the cycle time by 78.36%, also with negligible cost increase with respect to Case A. Therefore, we conclude that increasing the heat exchange surface area is generally more efficient and cost-effective than increasing the PCM's conductivity.

The economic assessment of the prototype hereby analyzed is as important as the technical evaluation for its development into a commercial form. In particular, manufacturing a 1.16 kWh prototype of the type A requires the following material costs:

- 1.93 kg Hydralloy $C_5$ powder: €386 [29],
- 2.98 kg PCM (Pluss OM35): €46.93 [50],
- 1.2 m-long 2 mm-thick aluminum tube: €8,

for a total of €440 per single prototype, with an estimated specific cost of about 380 €/kWh, and 288 €/$kW_{discharge}$. Such costs must be increased when considering local hydrogen production and possible compression in a gas buffer tank, if needed. We can disregard the weight of piping and instrumentation on the specific costs. Prototypes B and C entail very similar expenses, except for possible manufacturing costs for the fins on the aluminum tubes. For comparison, Li-Ion batteries' specific costs were reported in the range 100 ÷ 140 $/kWh as of 2021, with an expected value in the range 70 ÷ 90 $/kWh by 2050 [51–53]. Nonetheless, electrochemical storage is not suitable for seasonal or long-term energy storage, in contrast to hydrogen. We also comment that the costs of an individual prototype are expected to significantly reduce with economies of scale.

## 5. Conclusions

In order to boost the performance of the passive heat management of metal hydride-based hydrogen storage systems, this study assessed the performance of five MH–PCM hydrogen storage configurations (bare cylinder, longitudinal finned design, transversal finned design, bare helix, and finned helix) in terms of cycle time, charge/discharge power, and power density. Key findings include:

- fins significantly accelerate thermal exchange, reducing storage cycle times by up to 80.6% compared to a bare cylinder.
- at high Biot numbers, i.e., finned designs, PCM properties no longer constrain performance. Instead, MH conductivity becomes the bottleneck;
- the finned helix design exhibits the best performance, with a volume energy density of 6.13 $kg_{H_2}/m^3$, a charge/discharge power of 6.75 kW and 13.25 kW, and a power density of 2.55 kW/kg;
- expanded graphite improves kinetics in low conductivity designs, cutting ab/desorption times by 10% and 31%, respectively, but provides negligible benefits in finned configurations. Moreover, the introduction of expanded graphite in the hydride powder reduces the hydrogen storage capacity;
- the cycle time (i.e., cycling between 0.5% and 99.5% in $H_2$ storage capacity) is reduced from 154 min in the bare cylinder design to 15.7 min in the helix-shaped design.

These results demonstrate that performance optimization requires prioritizing geometry-driven heat-transfer improvements, complemented by selective material enhancements when heat conduction remains a limiting factor. The insights provide practical design rules to maximize the efficiency and power output of MH–PCM storage systems, directly supporting their integration in fuel cell electric vehicles and decentralized renewable energy systems. Nonetheless, key limitations must be acknowledged. We disregarded the

impact of self-densification and pulverization inside the hydride powder, which affects the hydrogen storage capacity, as well as the lifetime of the powder in terms of the number of cycles and degradation rates. To this aim, the authors see experimental validation of the numerical results and the evaluation of such assumptions as the most relevant follow-up to this work. In particular, the bare and transversally finned cylinders (Cases A and C) will be tested under the same operational conditions, hereby described (40 bar inlet pressure, Hydralloy C5, low-temperature paraffins), using the same geometrical design, to assess the real performances in terms of cycle time. A hydrogen mass flow meter and a series of thermocouples inside the PCM will be used to measure the equivalent charge and discharge powers and to track the liquefaction front, respectively. This first round of experiments will give us an estimate of the error of the numerical model.

**Author Contributions:** M.M.: Methodology, Software, Writing—Original Draft, Visualization. G.F.: Conceptualization, Supervision, Data Curation, Writing—Review and Editing. A.L.F. Conceptualization, Supervision, Writing—Review and Editing, Funding acquisition. S.U.: Writing—Review and Editing, Project Administration. All authors have read and agreed to the published version of the manuscript.

**Funding:** This project has been partially supported by the following projects: PRIN P20223JMB3—Modeling and optimization of sustainable hydrogen refueling infrastructures (HyREFI) and PRIN 2020BFX8JY—Hybrid Sustainable Mobility (HYSUM); ECS 0000024 Rome Technopole, CUP B83C22002820006, National Recovery and Resilience Plan (NRRP) Mission 4 Component 2 Investment 1.5, funded by the European Union—NextGenerationEU; National Recovery and Resilience Plan (NRRP), Mission 4 Component 2 Investment 1.3—Call for tender No. 1561 of 11 October 2022 of Ministero dell'Università e della Ricerca (MUR); funded by the European Union—NextGenerationEU.

**Data Availability Statement:** The original contributions presented in this study are included in the article. Further inquiries can be directed to the corresponding author.

**Conflicts of Interest:** The authors declare no conflicts of interest.

## References

1. European Commission. A Clean Planet for All—A European Strategic Long-Term Vision for a Prosperous, Modern, Competitive and Climate Neutral Economy, 2018. Available online: https://eur-lex.europa.eu/legal-content/EN/TXT/PDF/?uri=CELEX:52018DC0773&from=EN (accessed on 23 May 2022).
2. United Nations—Department of Economic and Social Affairs. The 17 Goals, 2015. Available online: https://sdgs.un.org/goals (accessed on 23 May 2022).
3. Ubertini, S.; Facci, A.L.; Andreassi, L. Hybrid hydrogen and mechanical distributed energy storage. *Energies* **2017**, *10*, 2035. [CrossRef]
4. Facci, A.L.; Ubertini, S. Analysis of a fuel cell combined heat and power plant under realistic smart management scenarios. *Appl. Energy* **2018**, *216*, 60–72. [CrossRef]
5. Hossain, E.; Faruque, H.M.R.; Sunny, M.S.H.; Mohammad, N.; Nawar, N. A Comprehensive Review on Energy Storage Systems: Types, Comparison, Current Scenario, Applications, Barriers, and Potential Solutions, Policies, and Future Prospects. *Energies* **2020**, *13*, 36514. [CrossRef]
6. Al Kareem, S.S.A.; Hassan, Q.; Fakhruldeen, H.F.; Hanoon, T.M.; Jabbar, F.I.; Algburi, S.; Khalaf, D.H. A review on physical and chemical hydrogen storage methods for sustainable energy applications. *Unconv. Resour.* **2025**, *8*, 100235. [CrossRef]
7. Zhang, Y.; Campana, P.E.; Lundblad, A.; Yan, J. Comparative study of hydrogen storage and battery storage in grid connected photovoltaic system: Storage sizing and rule-based operation. *Appl. Energy* **2017**, *201*, 397–411. [CrossRef]
8. Ye, Y.; Zhu, H.; Cheng, H.; Miao, H.; Ding, J.; Wang, W. Performance optimization of metal hydride hydrogen storage reactors based on PCM thermal management. *Appl. Energy* **2023**, *338*, 120923. [CrossRef]
9. Niaz, S.; Manzoor, T.; Pandith, A.H. Hydrogen storage: Materials, methods and perspectives. *Renew. Sustain. Energy Rev.* **2015**, *50*, 457–469. [CrossRef]
10. Patil, S.D.; Gopal, M.R. Analysis of a metal hydride reactor for hydrogen storage. *Int. J. Hydrogen Energy* **2013**, *38*, 942–951. [CrossRef]

11. Bartolucci, L.; Krastev, V.K. *On the Thermal Integration of Metal Hydrides with Phase Change Materials: Numerical Simulation Developments Towards Advanced Designs*; SAE Technical Paper 022-24-0018; SAE: Warrendale, PA, USA, 2022.
12. Kumar, A.; Muthukumar, P. Experimental investigation on hydrogen transfer in coupled metal hydride reactors for multistage hydrogen purification application. *Appl. Energy* **2024**, *363*, 123076. [CrossRef]
13. Wimmer, A.; Linder, M.; Bürger, I. Metal hydride-based cooling system for fuel cell electric vehicles: Achieving a temperature lift of 40 K. *Appl. Energy* **2025**, *398*, 126396. [CrossRef]
14. Proia, P.; Sbragaglia, M.; Falcucci, G. Melting with natural convection with heterogeneous heating sources. *Appl. Therm. Eng.* **2024**, *257*, 124089. [CrossRef]
15. Kotowicz, J.; Uchman, W.; Jurczyk, M.; Sekret, R. Evaluation of the potential for distributed generation of green hydrogen using metal-hydride storage methods. *Appl. Energy* **2023**, *344*, 121269. [CrossRef]
16. Mendecka, B.; Ilio, G.D.; Krastev, V.K.; Bella, G. Technical assessment of phase change material thermal expansion for passive solar tracking in residential thermal energy storage applications. *J. Energy Storage* **2022**, *48*, 103990. [CrossRef]
17. Mendecka, B.; Ilio, G.D.; Krastev, V.K.; Bella, G. Evaluating the potential of phase-change induced volumetric expansion in thermal energy storage media for passive solar tracking in high-temperature solar energy systems. *Appl. Therm. Eng.* **2022**, *212*, 118561. [CrossRef]
18. Lewis, S.D.; Chippar, P. Analysis of heat and mass transfer during charging and discharging in a metal hydride-phase change material reactor. *J. Energy Storage* **2021**, *33*, 102108. [CrossRef]
19. Marty, P.; de Rango, P.; Delhomme, B.; Garrier, S. Various tools for optimizing large scale magnesium hydride storage. *J. Alloy. Compd.* **2013**, *580*, S324–S328. [CrossRef]
20. Bouzgarrou, F.; Mellouli, S.; Alqahtani, T.; Algarni, S. Parametric study of a metal hydride reactor with phase change materials and heat pipes. *Int. J. Energy Res.* **2021** , *46*, 4588–4598. [CrossRef]
21. Mellouli, S.; Alqahtani, T.; Algarni, S.; Askrid, F.; Naimia, S. Numerical simulation of a combined thermochemical-latent energy storage system based on paired metal hydrides and phase change material. *J. Energy Storage* **2024**, *46*, 4588–4598. [CrossRef]
22. Dong, X.; Zhao, H.; Li, H.; Fucucci, G.; Zheng, Q.; Zhao, H.; Pu, J. A novel design of a metal hydride reactor integrated with phase change material for H2 storage. *Appl. Energy* **2024**, *367*, 123321. [CrossRef]
23. Larpruenrudee, P.; Bennett, N.S.; Fitch, R.; Sauret, E.; Gu, Y.; Islam, M.S. Investigation of metal hydride hydrogen storage performance using phase change materials. *Int. J. Hydrogen Energy* **2024**, *60*, 996–1019. [CrossRef]
24. Shrivastav, A.P.; Kanti, P.K.; Mohan, G.; Maiya, M. Design and optimization of metal hydride reactor with phase change material using fin factor for hydrogen storage. *J. Energy Storage* **2024**, *77*, 109975. [CrossRef]
25. Nyamsi, S.N.; Tolj, I. Metal hydride reactors and phase change materials: Enhancing energy storage for medium-high power vehicles. *J. Energy Storage* **2024**, *104*, 114545. [CrossRef]
26. Bao, Z. Performance investigation and optimization of metal hydride reactors for high temperature thermochemical heat storage. *Int. J. Hydrogen Energy* **2015**, *40*, 5664–5676. [CrossRef]
27. Maggini, M.; Falcucci, G.; Rosati, A.; Ubertini, S.; Facci, A.L. Non-Dimensional Numerical Analysis of Coupled Metal Hydride - Phase Change Material Hydrogen Storage System. *J. Energy Storage* **2024**, *93*, 112230. [CrossRef]
28. Melnik, D.; Bürger, I.; Mitzel, J.; Käß, J.; Sarkezi-Selsky, P.; Jahnke, T.; Knöri, T. Energy efficient cold start of a Polymer Electrolyte Membrane Fuel Cell coupled to a thermochemical metal hydride preheater. *Appl. Energy* **2024**, *359*, 122585. [CrossRef]
29. AMG Titanium GfE Gesellschaft für Elektrometallurgie mbH. Energy Supply with Hydralloy C. 2025. Available online: https://www.gfe.com/en/products-and-solutions/alloys (accessed on 11 November 2025 ).
30. Maggini, M.; Facci, A.L.; Falcucci, G.; Ubertini, S. Numerical Modeling of Metal Hydride-Phase Change Material Hydrogen Storage Systems with Increased Heat Exchange surface area. *Appl. Energy* **2025**, *378*, 124725. [CrossRef]
31. Ye, Y.; Ding, J.; Wang, W.; Yan, J. The storage performance of metal hydride hydrogen storage tanks with reaction heat recovery by phase change materials. *Appl. Energy* **2021**, *299*, 117255. [CrossRef]
32. Lin, X.; Zhu, Q.; Leng, H.; Yang, H.; Lyu, T.; Li, Q. Numerical analysis of the effects of pArticle radius and porosity on hydrogen absorption performances in metal hydride tank. *Appl. Energy* **2019**, *250*, 1065–1072. [CrossRef]
33. Chaise, A.; de Rango, P.; Marty, P.; Fruchart, D. Experimental and numerical study of a magnesium hydride tank. *Int. J. Hydrogen Energy* **2010**, *35*, 6311–6322. [CrossRef]
34. Bao, Z.; Yang, F.; Wu, Z.; Cao, X.; Zhang, Z. Simulation studies on heat and mass transfer in high-temperature magnesium hydride. *Appl. Energy* **2013**, *112*, 1181–1189. [CrossRef]
35. S.Mellouli.; Abhilash, E.; Askri, F.; Nasrallah, S.B. Integration of thermal energy storage unit in a metal hydride hydrogen storage tank. *Appl. Therm. Eng.* **2016**, *102*, 1185–1196. [CrossRef]
36. Jemni, A.; Nasrallah, S.B. Study of two-dimensional heat and mass transfer during absorption in metal-hydrogen reactor. *Int. J. Hydrogen Energy* **1995**, *20*, 43–52. [CrossRef]
37. Talaganis, B.; Meyer, G.; Aguirre, P. Modeling and simulation of absorption–desorption cyclic processes for hydrogen storage-compression using metal hydrides. *Int. J. Hydrogen Energy* **2011**, *36*, 13621–13631. [CrossRef]

38. Kim, J.S.; Han, W.B.; Cho, H.S.; Jeong, M.S.; Jeong, S.U.; Cho, W.C.; Kang, K.S.; Kim, C.H.; Bae, K.K.; Kim, J.W.; et al. Hydrogen Storage and Release Properties for Compacted Ti-Mn Alloy. *Korean Hydrog. New Energy Soc.* **2017**, *28*, 9–16. [CrossRef]
39. Sreeraj, R.; Aadhithiyan, A.; Anbarasu, S. Integration of thermal augmentation methods in hydride beds for metal hydride based hydrogen storage systems: Review and recommendation. *J. Energy Storage* **2022**, *52*, 105039. [CrossRef]
40. Voller, V.; Cross, M. Accurate solutions of moving boundary problems using the enthalpy method. *Int. J. Heat Mass Transf.* **1981**, *24*, 545–556. [CrossRef]
41. Tao, Y.; He, Y. Effects of natural convection on latent heat storage performance of salt in a horizontal concentric tube. *Appl. Energy* **2015**, *143*, 38–46. [CrossRef]
42. Tang, Y.; Su, D.; Huang, X.; Alva, G.; Liu, L.; Fang, G. Synthesis and thermal properties of the MA/HDPE composites with nano-additives as form-stable PCM with improved thermal conductivity. *Appl. Energy* **2016**, *180*, 116–129. [CrossRef]
43. Pietrak, K.; Wisniewski, T.S. A review of models for effective thermal conductivity of composite materials. *J. Power Technol.* **2015**, *95*, 14–24.
44. Fluent User Manual. 2025. Available online: https://www.afs.enea.it/project/neptunius/docs/fluent/html/ug/main_pre.htm (accessed on 25 October 2025).
45. V.M.Skripnyuk.; M.Ron. Hydrogen desorption kinetics in intermetallic compounds C2, C51 and C52 with Laves phase structure. *Int. J. Hydrogen Energy* **2003**, *28*, 303–309. [CrossRef]
46. Kölbig, M.; Bürger, I.; Linder, M. Characterization of metal hydrides for thermal applications in vehicles below 0 °C. *Int. J. Hydrogen Energy* **2019**, *44*, 4878–4888. [CrossRef]
47. Laurencelle, F.; Goyette, J. Simulation of heat transfer in a metal hydride reactor with aluminium foam. *Int. J. Hydrogen Energy* **2007**, *32*, 2957–2964. [CrossRef]
48. Lake, A.; Rezaie, B. Energy and exergy efficiencies assessment for a stratified cold thermal energy storage. *Appl. Energy* **2018**, *220*, 605–615. [CrossRef]
49. Liu, S.; Ahmadi-Senichault, A.; Pozzobon, V.; Lachaud, J. Multi-scale investigation of heat and momentum transfer in packed-bed TES systems up to 800 K. *Appl. Energy* **2024**, *366*, 123285. [CrossRef]
50. savE PCMs Product Range. 2025. Available online: https://plussat.eu/save-pcm-product-range/?_type=organic-mixture (accessed on 28 November 2025).
51. Mauler, L.; Duffner, F.; Zeier, W.G.; Leker, J. Battery cost forecasting: A review of methods and results with an outlook to 2050. *Energy Environ. Sci.* **2021**, *14*, 4712–4739. [CrossRef]
52. Rosati, A.; Facci, A.L.; Ubertini, S. Techno-economic analysis of battery electricity storage towards self-sufficient buildings. *Energy Convers. Manag.* **2022**, *256*, 115313. [CrossRef]
53. Vatankhah Ghadim, H.; Haas, J.; Breyer, C.; Gils, H.C.; Read, E.G.; Xiao, M.; Peer, R. Are we too pessimistic? Cost projections for solar photovoltaics, wind power, and batteries are over-estimating actual costs globally. *Appl. Energy* **2025**, *390*, 125856. [CrossRef]